JOURNAL OF SYNCHROTRON RADIATION

ISSN 1600-5775

Received 24 September 2019
Accepted 22 January 2020

Edited by I. Lindau, SLAC/Stanford University, USA

Keywords: XANES nanoscopy; undulator beamlines; chemical distribution mapping; tomography.

Development of XANES nanoscopy on BL7C at PLS-II

Jae Yeon Park, Jitendra Pal Singh, Jun Lim and Sangsul Lee*

Pohang Accelerator Laboratory, POSTECH, Jigokro 127, Pohang, Kyungbuk 37637, South Korea.
*Correspondence e-mail: sangsul@postech.ac.kr

X-ray absorption near-edge structure (XANES) imaging is a powerful tool to visualize the chemical state distribution of transition-metal-based materials at synchrotron radiation facilities. In recent years, the electrochemical working rechargeable battery has been the most studied material in XANES imaging owing to the large increase of portable electronics and electric vehicles. This work acknowledges the importance of battery analysis and has developed the XANES imaging system on BL7C at Pohang Light Source-II (PLS-II). BL7C employs an undulator taper configuration to obtain an energy band >130 eV near the *K*-absorption edge of the target element with a minimum energy interval >0.2 eV. While measuring energy-dependent images, the zone plate translation maintains the best focus, and then various data processes such as background correction, image registration and clustering allow single XANES spectrum extraction and chemical distribution mapping. Here, the XANES imaging process is described, the XANES spectrum quality is identified and the chemical states of the partially charged cathode material used in lithium-ion batteries as an application example are examined.

1. Introduction

Synchrotron radiation facilities have developed X-ray absorption near-edge structure (XANES) imaging over the last 30 years (Kinney *et al.*, 1986; Andrews *et al.*, 2010). XANES spectroscopy was already accepted as an established technique in surface and molecular science (Bianconi, 1980); thus, XANES microscopy was expected to provide more detailed information for micrometre-sized specimens. Since then, with the fabrication development of the X-ray Fresnel zone plate, spatial resolution of up to 30 nm has been achieved (de Smit *et al.*, 2008). The advent of charged-coupled devices (CCDs) with high quantum efficiency has increased the energy resolution to 0.1 eV (Chen *et al.*, 2015). Moreover, computer language related to image processing supports finer spectrum extraction and chemical distribution mapping (Meirer *et al.*, 2013). This technical growth has widely expanded the application area from academic fields such as chemistry (Ade *et al.*, 1992), biology (Wang *et al.*, 2015) and geophysics (De Andrade *et al.*, 2011) to industrial areas such as art (Cotte *et al.*, 2010), medicine (James *et al.*, 2016) and electronics (Yu *et al.*, 2018). In recent years, electronic energy storage materials have become one of the most important research materials because study of their electrochemical state distribution is closely related to improving the energy storage capability, lifetime, safety and manufacturing cost (Shearing *et al.*, 2011; Bak *et al.*, 2018; Johannes *et al.*, 2017; Wang *et al.*, 2014). With the increasing number of studies on battery imaging, we have contrived XANES imaging by utilizing the synchrotron beamline for battery-material analysis.

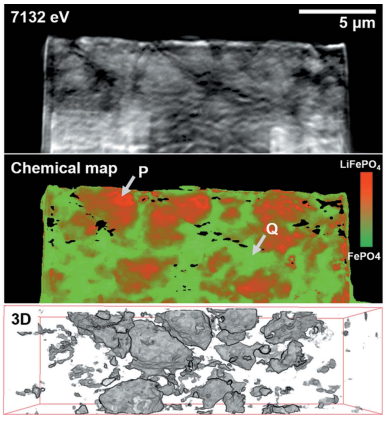

BL7C at Pohang Light Source-II (PLS-II) has already provided nanotomography using full-field hard X-ray transmittance imaging based on the objective zone plate. In the beamline, X-ray sources are generated from the undulator, and a monochromatic X-ray is selected by two parallel silicon crystals. BL7C can easily acquire energy-dependent images using these instruments, but we need to address certain challenges. First, we have to secure the wide energy band over about 100 eV. In the undulator beamline, the undulator tapering method (Sung *et al.*, 2014) is required to maintain higher intensity X-rays between tens of eV. The wider energy band allows detection of the *K*-edge XANES spectrum. The X-ray energy range of BL7C covers the *K*-edge of transition metals such as Mn, Fe and Co. These elements are the major components of electrochemical working batteries and their chemical states reflect their oxidation states. Second, the energy-dependent images are defocused while their energy changes, because the focal length of the objective zone plate employed as diffraction optics is dependent on the X-ray energy. The zone plate position is corrected with energy changes and the image is then resized so that the sample on the image can be moved, thus image registration is required (Liu *et al.*, 2012). Moreover, various other imaging processes should be used to extract the XANES spectrum on a single pixel of an image dataset. This information mining process is accompanied by computational methods due to its effectiveness in various X-ray imaging techniques (Mao *et al.*, 2019; Zhang *et al.*, 2017). We need to compare it with bulk XANES spectroscopy to confirm its accuracy. The final goal is to analyze the battery materials with chemical distribution mapping, which represents the meaningful values of the pixel (main absorption-edge energy or charging/discharging ratio). This work involves statistical mathematics and computer programming to handle millions of spectra.

In this paper, we demonstrate the development progress of XANES nanoscopy. A single XANES spectrum is identified with iron oxide particles that are tens of micrometres in size, and the XANES nanoscopy of the cathode material of a lithium-ion battery (LIB) is provided as an application example.

2. XANES nanoscopy installation

XANES nanoscopy is installed on BL7C which has already established zone-plate-based hard X-ray full-field transmission microscopy (Lee *et al.*, 2017). Fig. 1 shows the overall setup of the beamline from the front-end of the storage ring to the X-ray image detector in the experimental hutch. Synchrotron X-ray radiation is generated in the conventional hybrid-type in-vacuum undulator (Kim *et al.*, 2016). The X-ray beam profile depends on the gap and the tapering between the magnet arrays of the undulator in the vacuum system. The planar undulator (planar mode) maximizes the photon flux at a specific energy and the tapered configuration (tapered mode) permits a wide spectral range (Sung *et al.*, 2014).

The liquid-nitrogen-cooled double-crystal monochromator (DCM) selects the monochromatic energy of the undulator radiation in the energy range 5–15 keV, covering the *K*-absorption edge of transition metals such as Mn, Fe and Co. The energy interval is 2–0.2 eV. The rhodium-coated horizontal focusing plane mirror (HFM) and the vertical focusing plane mirror (VFM) focus the monochromatic beam. The focused beam profile is monitored in front of the sample stage using the X-ray beam position monitor (XBPM) with the feedback system (Park *et al.*, 2018). This feedback system maintains the beam position during the energy change caused by the change in monochromator angle. The sample position is controlled using the linear stages with 27 mm travel length and 0.2 µm directional repeatability. This linear stage with an encoding function is useful for returning to the sample position after measuring the background. The tomographic experiment uses an air bearing rotation stage with <0.001° angular resolution.

The objective Fresnel zone plate magnifies an X-ray transmittance image in the off-axis illumination system. The X-ray image is converted to the visible range in the thin scintillation crystal (15 µm-thick Tb:LSO), re-magnified by the 20× optical objective and then measured by the CCD detector (1024 × 1024 pixels, Princeton Instrument). The field of view (FOV) and spatial resolution are variable in their respective ranges 30–300 µm and 30–300 nm, following the outermost zone width of a zone plate (Lim *et al.*, 2018). The XANES imaging experiment accumulates projection images with an energy series and the accumulated images are then processed to extract a single XANES spectrum in a single pixel. Finally, the spectroscopic image data determines the chemical state distribution.

3. Undulator configuration

The broad energy band is optimized from the tapered configuration of the undulator. Fig. 2 shows the normalized X-ray intensity measured by the XBPM for different conditions of the tapering at around the Fe *K*-absorption edge. The

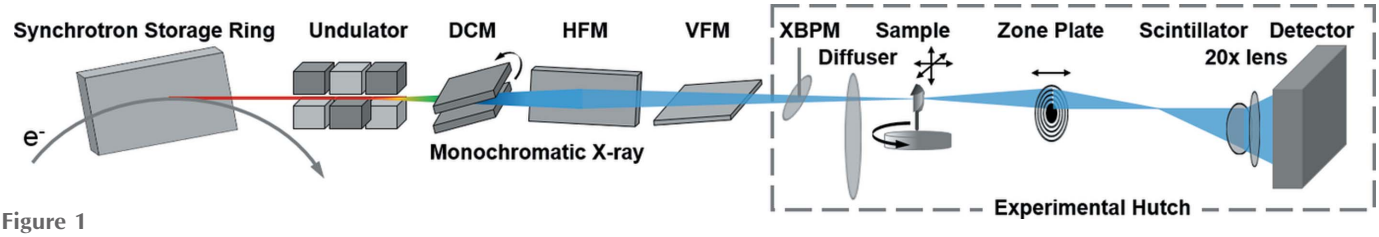

Figure 1
Installation diagram of XANES nanoscopy on BL7C.

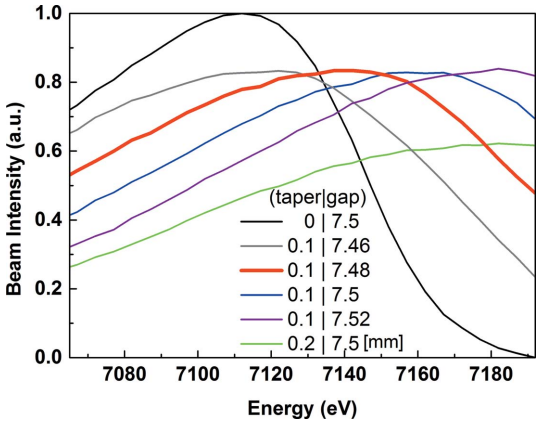

Figure 2
Tapered configuration of the undulator.

planar mode (taper 0 mm and gap 7.5 mm) has the highest intensity and narrowest bandwidth. The greater the undulator tapering, the wider the spectral width, but the peak intensity decreases as the peak position shifts to a higher energy. The optimal condition is determined at taper 0.1 mm and gap 7.48 mm (the red line in Fig. 2). The energy range covers −50 eV to +80 eV at 7111 eV. Compared with the planar mode, the maximum intensity is decreased by about 20%, but the intensity fluctuation is more than twice as stable. This fluctuation is corrected in the background correction with other data processing. The tapered configuration also works almost identically at the *K*-absorption edge with other elements such as Mn, Co and Ni.

4. Image acquisition and data processing

XANES nanoscopy collects the images with different energies. At a single energy, a pair of images (sample image and background image) are measured to attain the background correction as shown in Fig. 3(*a*). This process subtracts the blank signal from all detected signals and blunts the intensity difference between different energies. The background-corrected image is converted to an absorbance image following the Beer–Lambert law [$A = -\ln(I/I_0)$, where I is the sample image and I_0 is the background image] with median filtering removing spot noise.

The first-order diffraction beam of the objective zone plate is used as an image beam following the lens formula between the sample, zone plate and detector (Michette *et al.*, 1992; Born & Wolf, 2013). The zone plate is employed as diffraction optics and changes its focal length with the energy. For instance, the focal length of the zone plate increases to about 7 mm while the X-ray energy increases by 130 eV using a zone plate with 150 µm diameter and 40 nm outermost zone width. To maintain the best focus, the zone plate has to translate away from the sample while the energy increases. However, although the translation stage is perfectly set on the beam axis, this translation causes movement of the sample and magnification at the nanoscale. Moved samples can be aligned using the phase-correction method, which is a well known technique for image registration and handling the image translation, rotation and scale using a Fourier transform as shown in Fig. 3(*b*) (Reddy & Chatterji, 1996; Gonzalez, 2011).

After background correction and image registration, the XANES spectrum can be extracted from single pixels of the

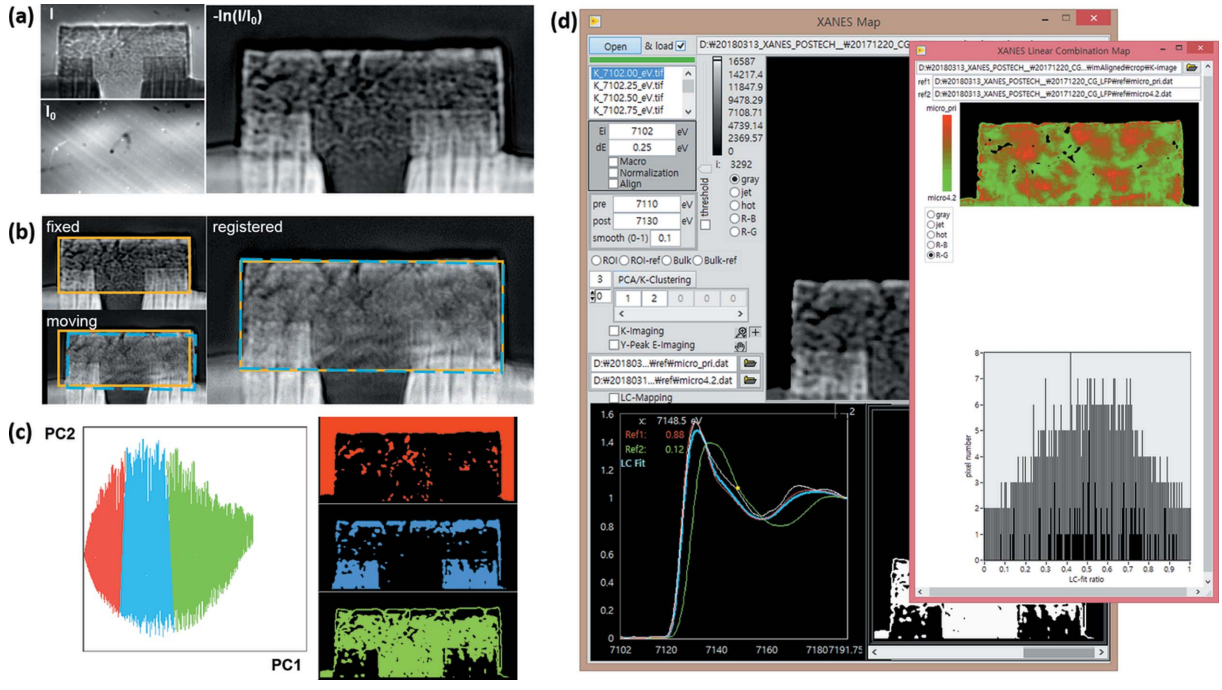

Figure 3
Image dataset process for chemical mapping with (*a*) background correction, (*b*) image registration, (*c*) PCA and *k*-means clustering combination, and (*d*) the laboratory-made auto-processing software on *LabView*.

energy-dependent images. The XANES imaging dataset has millions of spectra because it uses a CCD detector with 1024 × 1024 pixels. Among numerous spectra, the sample spectra only participate in the chemical state mapping. Therefore, a statistical method for differentiating the sample spectra is required. Principal component analysis (PCA) is a widely used statistical technique for reducing data dimensions, using an orthogonal transformation to convert the coordination of original data into the coordination of principal component data (Jolliffe & Cadima, 2016). PCA can reduce the XANES imaging dataset in four dimensions (*xy* coordinates, intensity and energy) into a two-dimensional PC coordinate (PC1 and PC2). PC coordinate data are arranged in order of spectral variance and trend and then partitioned into Voronoi cells to separate the sample spectra. The separation of sample spectra effectively segments the object image from others as shown in Fig. 3(*c*). This partitioning algorithm is *k*-means clustering, which is a commonly used data clustering technique (Arthur & Vassilvitskii, 2007).

XANES normalization is a typical method of regularizing data and is essential for comparing spectra directly. The bulk XANES spectrum has been normalized with pre-edge and post-edge line fitting (Teo, 1986). However, the single XANES spectrum of the image data has a higher noise level because the sample area that corresponds to a single pixel is much smaller than that measured by bulk XANES spectroscopy. In addition, the undulator beamline has a limited energy range. Therefore, polynomial fitting is employed for effective XANES normalization with the auto-normalization algorithm (Weng *et al.*, 2005). The spectrum fitting region consists of two parts: the first is from the first energy to the rising edge and the second is from the main edge peak to the last energy. This polynomial fitting method makes the background zero in the pre-edge and the last fitting value one.

The final goal of XANES imaging is to map the chemical state distribution. The chemical state of the proving element can be determined by calculating the influence level from reference materials. For example, the chemical state of a partially charged LIB can be determined using the linear combination (LC) fitting function with the pristine and the fully charged references. Their fitting results representing the charging ratio are mapped to the pixel value and the XANES map is displayed with the color legend as shown in Fig. 3(*d*).

The data techniques described previously are processed using the laboratory-made *LabView* program, which was developed to provide efficient analytics for extremely large datasets. Fig. 3(*d*) shows the front panel of the program displaying a simple user interface. This program reads common image formats such as TIF, SPE and PNG, and recognizes the X-ray energy in the filename. After processing the background correction and image registration in a series with the macro option checked, the dataset is loaded into primary memory. This memory loading allows us to display a single XANES spectrum with the mouse cursor positioning in real time. When the reference spectra are connected to the program, the LC-fitted spectrum and the chemical state value are shown together. XANES normalization requires each fitting point in the pre-edge and post-edge. The PCA and *k*-means clustering combination work with a partitioning number and the chemical map image then pops up with its histogram.

5. Signal comparison with bulk XANES spectroscopy

The XANES spectra at the Fe *K*-absorption edge provide detailed insights for the chemical states in the spectral trend of the pre-edge, the spectral shift of the main edge and the fluctuation of the post-edge. Thus, we prepared FeO particles to evaluate the performance of the XANES imaging on BL7C. Its optical thickness was determined to be about 20 µm by considering the absorption (Sciau & Wang, 2019). The particles were sprinkled on the carbon sheet and the sheet was held on the aluminium plate with a 10 mm-diameter hole; the plate was then installed on the sample stage.

We accumulated energy-dependent images of the FeO particles with XANES imaging. The energy range was −50 eV to +80 eV at the Fe^{2+} *K*-absorption edge of 7200 eV and the energy steps were 1 eV and 0.4 eV. The acquisition time for a single image was 1 s, and the scan for 380 energy points including the background measurement required about 40 min. The single energy image of the particle is displayed in the inset of Fig. 4(*a*). The XANES spectra were extracted from the particle region [red loop in the inset of Fig. 4(*a*)] through the previously described imaging data process and then

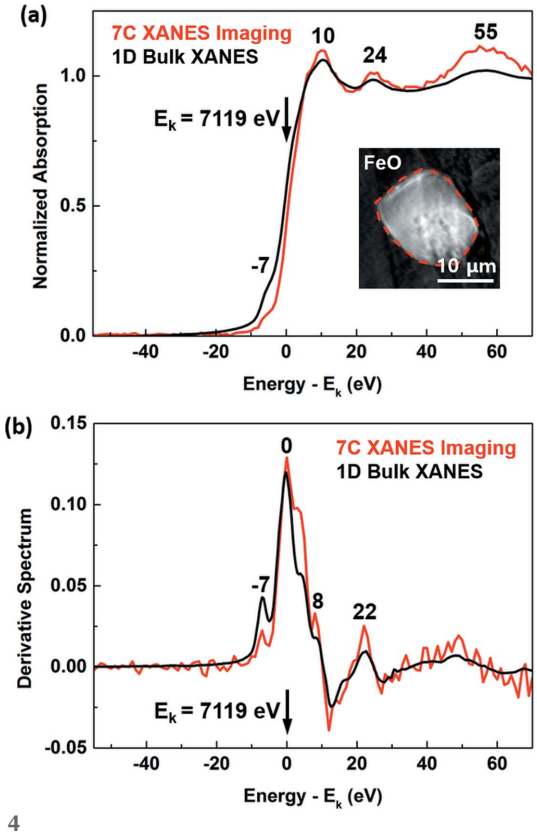

Figure 4
(*a*) XANES spectra and (*b*) their derivative spectra of FeO particles in XANES imaging at BL7C and XANES spectroscopy at BL1D.

averaged. The averaged XANES spectrum was compared with the bulk XANES spectrum as an appropriate standard to check the signal quality. The bulk XANES spectrum was measured from the bulk XANES spectroscopy beamline; the measurement area had numerous particles with local chemical heterogeneity and this could be the cause of the signal difference. Nevertheless, the two XANES spectra showed great agreement in the trend and peak positions. Normalization using polynomial fitting was perfectly plausible. The derivative spectra in Fig. 4(*b*) were well matched in the inflection points. It was confirmed that the undulator configuration and data processing for extracting a single XANES spectrum were successfully achieved.

6. Chemical mapping of an LIB cathode in XANES nanoscopy

A chemical map was produced from the cathode material of an $LiFePO_4$-based lithium-ion battery. The battery powder was galvanostatically charged and discharged at a 0.1 C rate after the fabrication processes. The cathode materials in the pristine 3.3 eV charged and fully charged states were carved to about 20 µm using a focused ion beam (FIB) system. The energy range was −20 eV to +80 eV at 7112 eV in energy steps of 1 eV. The acquisition time for a single image was 1 s and the whole scan for the FIB sample required about 20 min.

The cathode material was investigated using XANES imaging. The secondary particles of the cathode material had higher absorption at 7132 eV, as shown in Fig. 5(*a*). The metallic mount also had higher absorption. The absorption images were reconstructed to map the chemical distribution using the LC fitting function with the spectra of reference materials. The chemical map in Fig. 5(*b*) differentiated the chemical states between red (pristine; $LiFePO_4$) and green (fully charged; $FePO_4$). The nanometre-sized particles of the cathode material were charged and the few-micrometre-sized particles were partially charged. This map showed that the secondary particle size was influenced by the charging process. The charging difference was revealed from the single XANES spectrum presented in Fig. 5(*c*), which shows that the main edge shifts to higher energy and the absorption intensity decreases with charging. The charging area in a secondary particle is directly identified from the tomographic data in Fig. 5(*d*). A comparison between the chemical map and the tomographic image indicates that charging is undertaken from the particle surface.

7. Conclusions

XANES nanoscopy was developed on BL7C at PLS-II. In the undulator beamline, a tapered configuration was necessary to achieve a wide and stable energy band. It could improve beam stability by up to 80% with the potential for more, and extend the energy band from tens of eV to about 150 eV. Energy correction methods using background correction and image registration calibrated the energy fluctuation to extract a single XANES spectrum. The spectrum quality compared with that of the bulk XANES spectroscopy beamline corresponded well in terms of the peak position and fluctuation trend. The data processing technique that included PCA and *k*-means clustering combined with LC fitting achieved chemical mapping of the LIB cathode material. The mapping data showed the partially charged secondary particles and were comparable with tomographic data for structural analysis. All data acquisition and data processing were automated using the laboratory-made program *LabView*. In the future, XANES imaging studies on BL7C will be applied to visualize the chemical state of more varied transition-metal-based materials and will be improved for XANES tomography research in three-dimensional space.

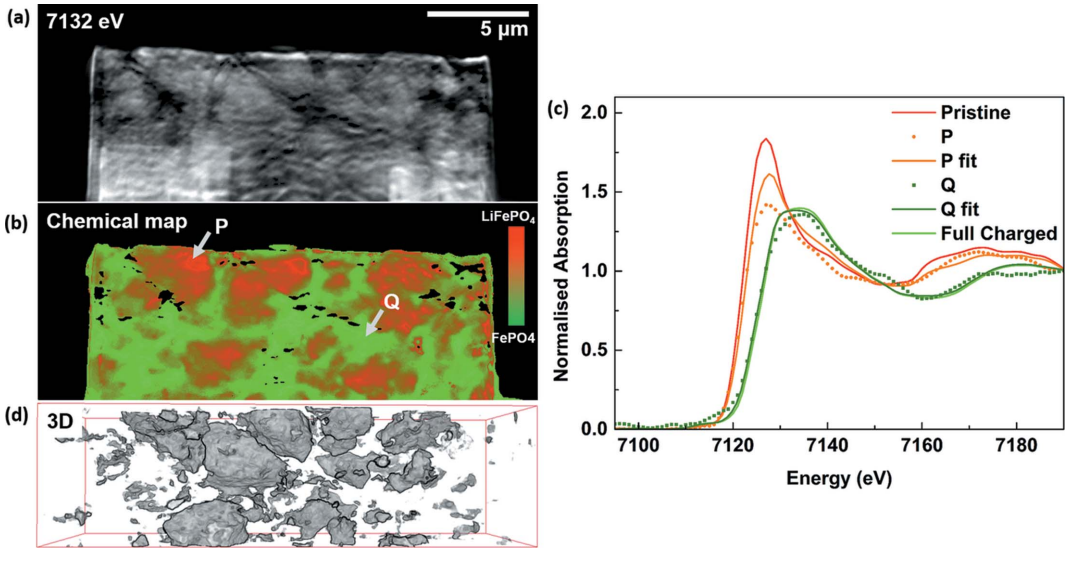

Figure 5
XANES mapping result of the charged cathode material of LIB. (*a*) Absorption image, (*b*) chemical distribution map, (*c*) LC-fitted spectra, (*d*) tomographic volume image of the cathode sample.

Funding information

This research was supported by the Basic Science Research Program through the National Research Foundation of Korea (NRF) and funded by the Ministry of Education (grant No. 2017R1C1B1011518).

References

Ade, H., Zhang, X., Cameron, S., Costello, C., Kirz, J. & Williams, S. (1992). *Science*, **258**, 972–975.

Andrews, J. C., Almeida, E., van der Meulen, M. C., Alwood, J. S., Lee, C., Liu, Y., Chen, J., Meirer, F., Feser, M., Gelb, J., Rudati, J., Tkachuk, A., Yun, W. & Pianetta, P. (2010). *Microsc. Microanal.* **16**, 327–336.

Arthur, D. & Vassilvitskii, S. (2007). *Proceedings of the Eighteenth Annual ACM-SIAM Symposium on Discrete Algorithms (SODA07)*, New Orleans, Louisiana, pp. 1027–1035. Philadelphia: Society for Industrial and Applied Mathematics.

Bak, S.-M., Shadike, Z., Lin, R., Yu, X. & Yang, X.-Q. (2018). *NPG Asia Mater.* **10**, 563–580.

Bianconi, A. (1980). *Appl. Surf. Sci.* **6**, 392–418.

Born, M. & Wolf, E. (2013). *Principles of Optics: Electromagnetic Theory of Propagation, Interference and Diffraction of Light.* Cambridge University Press.

Chen, X., Xiao, J., Wang, J., Deng, D., Hu, Y., Zhou, J., Yu, L., Heine, T., Pan, X. & Bao, X. (2015). *Chem. Sci.* **6**, 3262–3267.

Cotte, M., Susini, J., Dik, J. & Janssens, K. (2010). *Acc. Chem. Res.* **43**, 705–714.

De Andrade, V., Susini, J., Salomé, M., Beraldin, O., Rigault, C., Heymes, T., Lewin, E. & Vidal, O. (2011). *Anal. Chem.* **83**, 4220–4227.

Gonzalez, R. (2011). *Proceedings of the 26th International Conference on Image and Vision Computing New Zealand. (IVCNZ2011)*, 29 November–1st December 2011, Auckland, New Zealand.

James, S. A., Hare, D. J., Jenkins, N. L., de Jonge, M. D., Bush, A. I. & McColl, G. (2016). *Sci. Rep.* **6**, 20350.

Johannes, A., Salomon, D., Martinez-Criado, G., Glaser, M., Lugstein, A. & Ronning, C. (2017). *Sci. Adv.* **3**, eaao4044.

Jolliffe, I. T. & Cadima, J. (2016). *Philos. Trans. R. Soc. A*, **374**, 20150202.

Kim, D.-E., Lee, H.-H., Park, K.-H., Seo, H.-S., Ha, T., Jeong, Y.-G., Han, H.-S., Lee, W., Huang, J.-Y., Nam, S., Kim, K. & Shin, S. (2016). *J. Kor. Phys. Soc.* **69**, 903–908.

Kinney, J., Johnson, Q., Nichols, M. C., Bonse, U. & Nusshardt, R. (1986). *Appl. Opt.* **25**, 4583–4585.

Lee, S., Kwon, I., Kim, J.-Y., Yang, S.-S., Kang, S. & Lim, J. (2017). *J. Synchrotron Rad.* **24**, 1276–1282.

Lim, J., Lee, S., Park, J., Roh, Y. & Kim, Y. (2018). *Microsc. Microanal.* **24**, 262–263.

Liu, Y., Meirer, F., Williams, P. A., Wang, J., Andrews, J. C. & Pianetta, P. (2012). *J. Synchrotron Rad.* **19**, 281–287.

Mao, Y., Wang, X., Xia, S., Zhang, K., Wei, C., Bak, S., Shadike, Z., Liu, X., Yang, Y., Xu, R., Pianetta, P., Ermon, S., Stavitski, E., Zhao, K., Xu, Z., Lin, F., Yang, X., Hu, E. & Liu, Y. (2019). *Adv. Funct. Mater.* **29**, 1900247.

Meirer, F., Liu, Y., Pouyet, E., Fayard, B., Cotte, M., Sanchez, C., Andrews, J. C., Mehta, A. & Sciau, P. (2013). *J. Anal. At. Spectrom.* **28**, 1870–1883.

Michette, A. G., Morrison, G. R. & Buckley, C. J. (1992). *Springer Ser. Opt. Sci.* **67**, 293.

Park, J. Y., Kim, Y., Lee, S. & Lim, J. (2018). *J. Synchrotron Rad.* **25**, 869–873.

Reddy, B. S. & Chatterji, B. N. (1996). *IEEE Trans. Image Process.* **5**, 1266–1271.

Sciau, P. & Wang, T. (2019). In *Synchrotron Radiation*, edited by D. Joseph. IntechOpen.

Shearing, P., Wu, Y., Harris, S. J. & Brandon, N. (2011). *Interface Mag.* **20**, 43–47.

Smit, E. de, Swart, I., Creemer, J. F., Hoveling, G. H., Gilles, M. K., Tyliszczak, T., Kooyman, P. J., Zandbergen, H. W., Morin, C., Weckhuysen, B. M. & de Groot, F. M. F. (2008). *Nature*, **456**, 222–225.

Sung, N.-E., Lee, I.-J., Jeong, S. & Kang, S.-W. (2014). *J. Synchrotron Rad.* **21**, 1282–1287.

Teo, B. K. (1986). *EXAFS: Basic Principles and Data Analysis.* Berlin: Springer.

Wang, J., Chen-Wiegart, Y. & Wang, J. (2014). *Nat. Commun.* **5**, 4570.

Wang, P., Menzies, N. W., Lombi, E., McKenna, B. A., James, S., Tang, C. & Kopittke, P. M. (2015). *J. Exp. Bot.* **66**, 4795–4806.

Weng, T.-C., Waldo, G. S. & Penner-Hahn, J. E. (2005). *J. Synchrotron Rad.* **12**, 506–510.

Yu, Y.-S., Farmand, M., Kim, C., Liu, Y., Grey, C. P., Strobridge, F. C., Tyliszczak, T., Celestre, R., Denes, P., Joseph, J., Krishnan, H., Maia, F. R. N. C., Kilcoyne, A. L. D., Marchesini, S., Leite, T. P. C., Warwick, T., Padmore, H., Cabana, J. & Shapiro, D. A. (2018). *Nat. Commun.* **9**, 921.

Zhang, K., Ren, F., Wang, X., Hu, E., Xu, Y., Yang, X. Q., Li, H., Chen, L., Pianetta, P., Mehta, A., Yu, X. & Liu, Y. (2017). *Nano Lett.* **17**, 7782–7788.